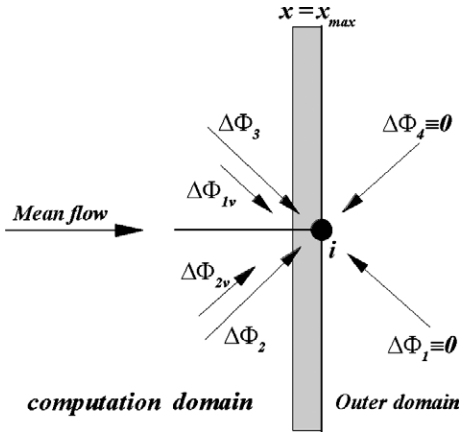

Fig. 8. Simple waves at a subsonic outflow boundary for models A and B.

2.4.1. Open domain boundary conditions

Let us assume that the subsonic boundary is an outflow boundary, as depicted in Fig. 8. Then, the only ingoing waves are ψ_1 and ψ_4. Therefore, the non-reflecting boundary condition will be the following:

$$\begin{cases} \Delta\Phi_1 \equiv 0 \\ \Delta\Phi_4 \equiv 0 \end{cases} \tag{20}$$

In other words, at every discrete point, i, situated on this boundary, the unknowns (the function and its derivatives) are updated only by the waves leaving the computation domain: $\psi_2, \psi_3, \psi_4, \psi_{1v}, \psi_{2v}$. The conditions (20) are merely introduced in (7) at the boundary points.

Although in a very simple form, this condition is effective as long as the background flow remains uniform (see numerical results in the subsequent section). However, when one considers the benchmark problem of the 2D shear-layer [6], spurious oscillations appear at the outflow boundary points, in the subsonic region. Indeed, the need to use a stretched grid in order to precisely capture the main properties of the shear-layer excites spurious waves in the solution and introduces additional numerical instabilities [7]. These instabilities first appear on the first derivatives. Later, these instabilities contaminate the primitive variables. At the supersonic outflow boundary, these oscillations leave the computation domain without any difficulty since all the simple waves leave the computation domain. However, in the subsonic region, some part of these oscillations remains in the calculation domain; this clearly means that conditions (20) are still poor in this case. To try to remedy this, we explicitly specify conditions (20) for the derivative variables: $r_\varphi, s_\varphi, \ldots$ More exactly, the condition $\Delta\Phi_1 \equiv 0$ stated for (r_φ, s_φ), for example, gives the following linear relation from (10):

$$s_p \cos\theta - r_p \sin\theta + r_u \sin^2\theta + s_v \cos^2\theta - \frac{1}{2}\sin 2\theta \times (s_u + r_v) = 0 \tag{21}$$

and the condition $\Delta\Phi_4 \equiv 0$ gives the following relation:

$$r_p \cos\theta + s_p \sin\theta - r_u \cos^2\theta - s_v \sin^2\theta - \frac{1}{2}\sin 2\theta \times (s_u + r_v) = 0 \tag{22}$$

Therefore, we have generated at each boundary point a set of two linear equations for the six discrete unknowns $(r_u, r_v, r_p, s_u, s_v, s_p)$. For example, if one selects r_u, r_v, s_u, s_v, as parameters, then the previous system can be solved for the discrete unknowns r_p and s_p at each boundary point, i, and for each time level $t_{n+1} \equiv (n+1)\Delta t$:

$$r_p|_i^{n+1} = (\sin\theta + \cos\theta)\left(1 - \frac{1}{2}\sin 2\theta\right) r_u|_i^{n+1} - \frac{1}{2}\sin 2\theta \times (\sin\theta - \cos\theta)(s_v + s_u + r_v)|_i^{n+1}$$

$$s_p|_i^{n+1} = (\sin\theta - \cos\theta)\left[s_v + \frac{1}{2}\sin 2\theta \times (s_v - r_u)\right]\Big|_i^{n+1} + \frac{1}{2}\sin 2\theta \times (\sin\theta + \cos\theta)(s_u + r_v)|_i^{n+1}$$

Therefore, instead of updating $(r_p, s_p)_i$ at $t = t_{n+1}$ by the general formula (7) we use the preceding solutions in which the remaining variables r_u, r_v, s_u, s_v are updated by (7). This kind of procedure is used in the benchmark problem of the 2D shear-layer, with interesting results (see the following numerical results).

Finally, if the boundary is a subsonic inflow boundary – unless there exists physical ingoing disturbances to specify at this boundary – the non-reflecting boundary conditions for model A or B are the following:

$$\begin{cases} \Delta\Phi_2 \equiv 0 \\ \Delta\Phi_3 \equiv 0 \\ \Delta\Phi_{1v} \equiv 0 \\ \Delta\Phi_{2v} \equiv 0 \end{cases} \tag{23}$$

Thus, this set of four linear equations makes it possible to solve for four discrete unknowns among the variables $(r_u, r_v, r_p, s_u, s_v, s_p)$, in order to get the equivalent of (21) and (22) for the Δ-P3 scheme.

2.4.2. Wall boundary conditions

To simplify our explanation, let us assume that the wall boundary is located along the line $x = x_{\max}$, Fig. 9. The only physical boundary condition for an inviscid flow near a hard wall is just the requirement that the velocity component normal to the wall vanishes. This condition, when it is used in conjunction with the governing equations, generates boundary conditions on the remaining variables. By considering the problem depicted in Fig. 9, it follows that $u \equiv 0$ and $M_x \equiv 0$ at every wall boundary point, P. Then, we get from (1) the following inferred condition for each point, P, on the wall:

$$r_p|_P^{n+1} + M_y \times s_u|_P^{n+1} = 0 \tag{24}$$

Then, the wall boundary conditions at every point, P, are the following:

$$\begin{aligned} u_P^{n+1} &\equiv 0 \\ r_p|_P^{n+1} &= -M_y \times s_u|_P^{n+1} \end{aligned} \tag{25}$$

The remaining variables are updated by the simple waves coming from the calculation domain: ψ_2, ψ_3, ψ_{1v}, ψ_{2v}, Fig. 9. In this way, no spurious waves are generated when acoustic or vorticity waves impinge the wall, since the waves entering the calculation domain (ψ_1, ψ_4) are set to zero in (7). Let us note that in the singular case, where the mean flow direction is aligned with the x-axis $(M_y \equiv 0)$, the wall boundary conditions which we derived are the same ones as those obtained in [1] in the case of the problem depicted in Fig. 9.

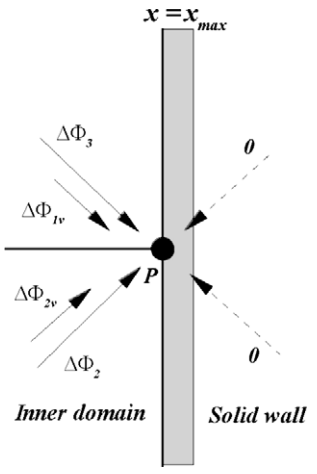

Fig. 9. Simple waves at a hard wall for models A and B.

Indeed, deduced from the locally simplified form of (1) at the boundary points, these conditions can be written as follows:

$$\begin{aligned} u &\equiv 0 \\ r_p &\equiv 0 \\ s_u &\equiv 0 \end{aligned} \tag{26}$$

To end this section, it is significant to note that although Δ-P3 scheme is more intricate than "standard numerical methods" such as DRP [8], or compact schemes [9], it generates boundary conditions much simpler than the ones customarily used in aeroacoustics [5]. It is one of the greatest advantages related to the use of an upwind scheme. By using our methodology, the implementation of the discretized boundary conditions in relation to the time-marching high-order scheme is easier; there is no need to use specific procedures such as ghost points. This fact has a positive impact on the overall accuracy and stability of the numerical solution. Before validating these procedures by numerical tests, let us briefly evoke the "evolution step" which combines the two preceding steps.

2.5. The evolution step for deriving a third-order scheme

We simply extend the procedure developed in [1] to the linear system (1). By defining φ as the generic variable which stands for u, v or p, we expand in Taylor series in time, $\varphi(x_i, y_i, t_n + \Delta t)$ (order 3) and its derivatives (order 2), around the basis point (x_i, y_i, t_n). Then, we substitute the temporal derivatives by their spatial counterparts, by applying a Cauchy–Kovaleskaya procedure. Finally, we truncate the previous series and we approximate the spatial derivatives by using the spatial interpolator, $\tilde{\varphi}(x, y)$. Then, we get a set of linear equations for the discrete unknowns $(\varphi, r_\varphi, s_\varphi)$ approximating (1).

For the primitive variables (u, v, p), these equations are:

$$\begin{cases} p_t|_i^n = -(r_u + s_v)|_i^n - (M_x r_p + M_y s_p)|_i^n \\ u_t|_i^n = -r_p|_i^n - (M_x r_u + M_y s_u)|_i^n \\ v_t|_i^n = -s_p|_i^n - (M_x r_v + M_y s_v)|_i^n \end{cases}$$
$$\begin{cases} p_{tt}|_i^n = -[(r_u)_t + (s_v)_t]|_i^n - (M_x (r_p)_t + M_y (s_p)_t)|_i^n \\ u_{tt}|_i^n = -(r_p)_t|_i^n - (M_x (r_u)_t + M_y (s_u)_t)|_i^n \\ v_{tt}|_i^n = -(s_p)_t|_i^n - (M_x (r_v)_t + M_y (s_v)_t)|_i^n \end{cases}$$
$$\begin{cases} p_{3t}|_i^n = [(\tilde{p}_{xx})_t + (\tilde{p}_{yy})_t]|_i^n + 2[M_x(\tilde{u}_{xxt} + \tilde{v}_{xyt}) + M_y(\tilde{u}_{xyt} + \tilde{v}_{yyt})]|_i^n + (M_x^2 \tilde{p}_{xxt} + 2M_x M_y \tilde{p}_{xyt} + M_y^2 \tilde{p}_{yyt})|_i^n \\ u_{3t}|_i^n = [(\tilde{u}_{xx})_t + (\tilde{v}_{xy})_t]|_i^n + 2[M_x(\tilde{p}_{xx})_t + M_y(\tilde{p}_{xy})_t]|_i^n + (M_x^2 \tilde{u}_{xxt} + 2M_x M_y \tilde{u}_{xyt} + M_y^2 \tilde{u}_{yyt})|_i^n \\ v_{3t}|_i^n = [(\tilde{u}_{xy})_t + (\tilde{v}_{yy})_t]|_i^n + 2[M_x(\tilde{p}_{xy})_t + M_y(\tilde{p}_{yy})_t]|_i^n + (M_x^2 \tilde{v}_{xxt} + 2M_x M_y \tilde{v}_{xyt} + M_y^2 \tilde{v}_{yyt})|_i^n \end{cases} \tag{27}$$

for the x-derivatives:

$$\begin{cases} (r_p)_t|_i^n = -(\tilde{u}_{xx} + \tilde{v}_{xy})|_i^n - (M_x \tilde{p}_{xx} + M_y \tilde{p}_{xy})|_i^n \\ (r_u)_t|_i^n = -\tilde{p}_{xx}|_i^n - (M_x \tilde{u}_{xx} + M_y \tilde{u}_{xy})|_i^n \\ (r_v)_t|_i^n = -\tilde{p}_{xy}|_i^n - (M_x \tilde{v}_{xx} + M_y \tilde{v}_{xy})|_i^n \end{cases}$$
$$\begin{cases} (r_p)_{tt}|_i^n = -[(\tilde{u}_{xx})_t + (\tilde{v}_{xy})_t]|_i^n - [M_x(\tilde{p}_{xx})_t + M_y(\tilde{p}_{xy})_t]|_i^n \\ (r_u)_{tt}|_i^n = -(\tilde{p}_{xx})_t|_i^n - [M_x(\tilde{u}_{xx})_t + M_y(\tilde{u}_{xy})_t]|_i^n \\ (r_v)_{tt}|_i^n = -(\tilde{p}_{xy})_t|_i^n - [M_x(\tilde{v}_{xx})_t + M_y(\tilde{v}_{xy})_t]|_i^n \end{cases} \tag{28}$$

and for the y-derivatives:

$$\begin{cases} (s_p)_t|_i^n = -(\tilde{u}_{xy} + \tilde{v}_{yy})|_i^n - (M_x\tilde{p}_{xy} + M_y\tilde{p}_{yy})|_i^n \\ (s_u)_t|_i^n = -\tilde{p}_{xy}|_i^n - (M_x\tilde{u}_{xy} + M_y\tilde{u}_{yy})|_i^n \\ (s_v)_t|_i^n = -\tilde{p}_{yy}|_i^n - (M_x\tilde{v}_{xy} + M_y\tilde{v}_{yy})|_i^n \end{cases}$$
$$\begin{cases} (s_p)_{tt}|_i^n = -[(\tilde{u}_{xy})_t + (\tilde{v}_{yy})_t]|_i^n - [M_x(\tilde{p}_{xy})_t + M_y(\tilde{p}_{yy})_t]|_i^n \\ (s_u)_{tt}|_i^n = -(\tilde{p}_{xy})_t|_i^n - [M_x(\tilde{u}_{xy})_t + M_y(\tilde{u}_{yy})_t]|_i^n \\ (s_v)_{tt}|_i^n = -(\tilde{p}_{yy})_t|_i^n - [M_x(\tilde{v}_{xy})_t + M_y(\tilde{v}_{yy})_t]|_i^n \end{cases} \quad (29)$$

All the time-derivatives appearing in (27)–(29) are broken up along each simple wave by using the six-wave model A ((10) and (13) with $\theta \equiv \pi/4$) or model B ($\theta \equiv A\tan(M_y/M_x)$). This makes it possible to identify the temporal fluctuation (or perturbation) brought by each wave. According to the flow regime and the direction of each wave, the fluctuations are shared and gathered at each discrete point, in order to update the data at this point. Fig. 4 depicts this procedure for models A and B.

However, the higher accuracy of this method is obtained at the cost of greater algorithm intricacy. Indeed, the time evolution requires the calculation of numerous high-order spatial derivatives in order to evolve in time the solution variables and several of their spatial derivatives. In this case, the computational effort per grid point per time-step can become very significant. Fortunately, the balancing factor that makes this scheme very competing is that relatively coarse grid resolution is sufficient to get a high accuracy. The preceding numerical experiments with Δ-P3 scheme [1] confirmed this fact.

3. Numerical results

Unless it is stated, a square grid with uniform spacing, h, in both spatial directions is employed. The global time-step, Δt, is defined by extending the one-dimensional CFL condition ($a\Delta t/\Delta x \leqslant 1$) to a 2D Cartesian uniform mesh. Indeed, we impose that the area swept during Δt by the fastest characteristic velocity, $(1 + \sqrt{M_x^2 + M_y^2})$, remains lower or equal to the area of the discrete cell defining the mesh (h^2). Then, this explicit CFL-like condition leads to the following inequality:

$$\pi \times \left[\Delta t \times \left(1 + \sqrt{M_x^2 + M_y^2}\right)\right]^2 \leqslant h^2$$

Then, by introducing the CFL (CFL $\leqslant 1$), the global time-step will be defined as

$$\Delta t \equiv \frac{h}{\sqrt{\pi}} \times \frac{\mathrm{CFL}}{1 + \sqrt{M_x^2 + M_y^2}} \quad (30)$$

Lastly, the derivatives used for computing the wave strengths, ψ_p, are calculated from formulae (18) and (19).

3.1. Axisymmetric pressure pulse

In this test-case, we test the effectiveness of the wave-models A and B defined in Section 2.2 as well as the radiation and outflow boundary conditions that we derived in Section 2.4. Our main goal is to order wave-models A and B used in the decomposition step. For this purpose, we solve the aeroacoustic equations, (1) ($H \equiv 0$), on the computation domain $[-1, 1]\times[-1, 1]$. An acoustic pulse is generated by an initial Gaussian pressure pulse distribution at the centre of the computation domain. The mean flow Mach number is defined by $\vec{M} \equiv (M_x, M_y)^t$. The wave front of the acoustic pulse expands radially; but because of the mean flow, the whole wave pattern is being convected downstream at the same time, without any distortion. The exact solution of this problem is reported in [8] and provides a reference to estimate the accuracy and the quality of the computed solutions. This problem is parametrized by the mean flow Mach number. Thus, two flow regimes are considered: a subsonic flow regime characterized by ($M_x = 0.8$, $M_y = 0.5$) and a supersonic one, distinguished by ($M_x = 2$, $M_y = 1$). The initial condition is as follows:

$$p(x,y) = e^{-20(x^2+y^2)}$$
$$u(x,y) = v(x,y) \equiv 0 \tag{31}$$

The initial conditions for the first-derivatives ($r_\varphi \equiv \varphi_x$, $s_\varphi \equiv \varphi_y$) are easily inferred from (31).

Now, we present the results of the simulations. Firstly, we consider the subsonic regime: $M_x = 0.8$, $M_y = 0.5$. The simulation time is $T = 2$ and the CFL number is 0.25. For each model, the maximum and the L_1-norm of the absolute error in pressure profile are calculated. Fig. 10 shows the grid convergence plots in L_1-norm for both models. As one can note it, the error levels are quite similar for both wave-models: in the subsonic regime, these models have similar behaviours. Therefore, the choice of the propagation angle does not seem to be decisive in such a case. In addition, a little reflection is found at the exit for both models (see Fig. 12, wave-model B); although this problem remains stable and confined as time grows up, it degrades the speed of convergence for both schemes, Fig. 10.

Fig. 11 provides comparisons between the computed and the exact pressure waveforms along the x-axis at $y = 0$, for the two wave models A and B. To obtain these results, only 10×10 grid points are necessary with the Δ-P3 scheme. Despite their differences in convergence, models A and B give identical waveforms. Besides, the quality of these results is maintained until the end of simulations. Fig. 12 shows the pressure contours for the acoustic pulse at various time levels in the simulation. The computation domain is divided into a 20×20 mesh and we use the wave model B for this simulation. The acoustic pulse leaves the computation domain through the top, bottom and right boundaries. As previously mentioned, some minor wiggles appear at the exit point $x = 1$, $y = -1$ for $t \geqslant 1.5$, indicating that the radiation boundary condition imposed in these regions is not entirely clear. However, one can note that the centre of the acoustic pulse is less than 20 mesh points away from the boundary. This limit value was found by Tam for this kind of problem in order to generate reflected wave amplitude less than 2% of the incident one [8]. We can remark that the expanding circles are circular, so that the computed acoustic wave speed is the same in all directions.

Now, let us examine the supersonic regime: $M_x = 2$, $M_y = 1$. The numerical solutions are obtained at $T = 0.125$ and $T = 0.375$ (Fig. 14). The CFL number is equal to 0.25. Fig. 13 shows the grid convergence plots in L_1-norm for both models. As one can see it immediately, the wave-model B produces a better convergence than the wave-model A: by selecting an arbitrary propagating direction free of the physics ($\theta = \pi/4$ for the wave-model A), the discrete points are updated independently of the direction of the mean-flow. This seems to result in a reduction of the rate of convergence for wave-model A. However, the quality of the results remains good for both models: wave-models A and B are comparable in terms of pressure levels, Fig. 14.

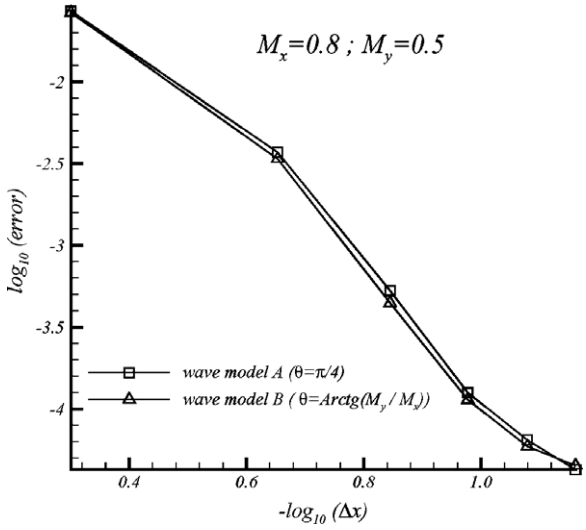

Fig. 10. Aeroacoustic equations. Grid convergence plot. Axi-symmetric pressure pulse in a non-stationary flow. Subsonic regime. $M_x = 0.8$, $M_y = 0.5$, $T = 2$.

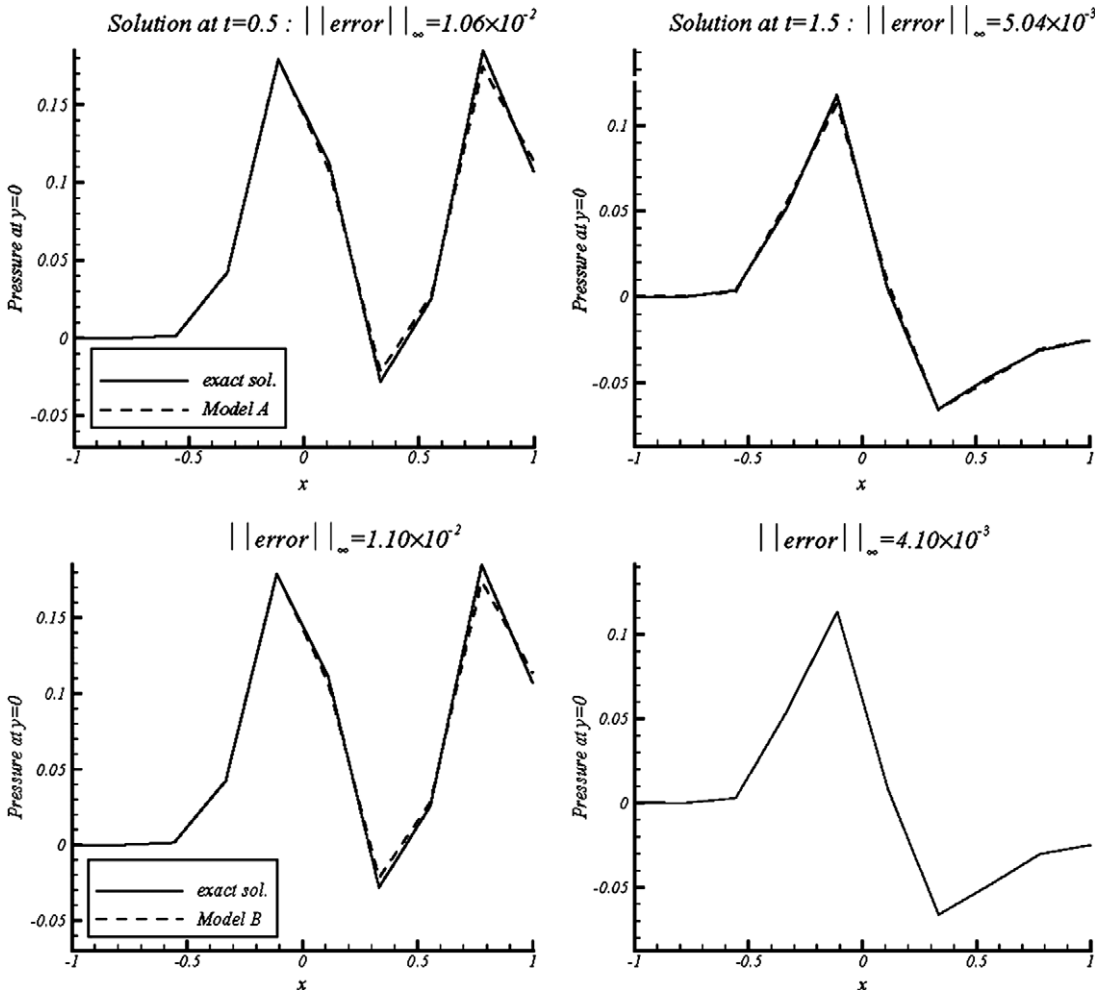

Fig. 11. Axi-symmetric pressure pulse. Pressure waveforms along the x-axis at $y = 0$. Subsonic regime: $M_x = 0.8$, $M_y = 0.5$. Top: wave model A, bottom: wave model B. 10×10 grid points, CFL = 0.25. Left: time $T = 0.5$; right: $T = 1.5$.

Lastly, Fig. 15 shows pressure contours for $M_x = 2$, $M_y = 1$. These results are obtained from wave model B on a 20×20 mesh. The acoustic pulse leaves the computation domain through the top and right boundaries. This simulation is easier to compute than the previous one, since the flow regime is supersonic. The non-reflecting boundary conditions are useless in such a case: all the simple waves, ψ_p, leave the computation domain. For this reason, no reflections are noticed at the boundaries, Fig. 15.

Therefore, in the supersonic regime the choice of the propagation angle becomes more important since physical information propagates in preferred directions. For this reason, the best results are obtained with a propagation direction aligned with the streamwise direction ($\theta \equiv A\tan(M_y/M_x)$) for model B. Overall, the results of these simulations suggest that we can rely on non-reflecting boundary conditions – whatever the wave-model – to yield accurate results. Furthermore, the resulting numerical scheme reproduces the wave speeds correctly. Wave models A and B yield stable schemes. For the tests considered, both models are similar in subsonic regimes.

3.2. Non-constant advection speed with source terms

In order to extend our procedure to linear aeroacoustics with a non-uniform mean flow and a source term, we consider the following scalar equation as a model:

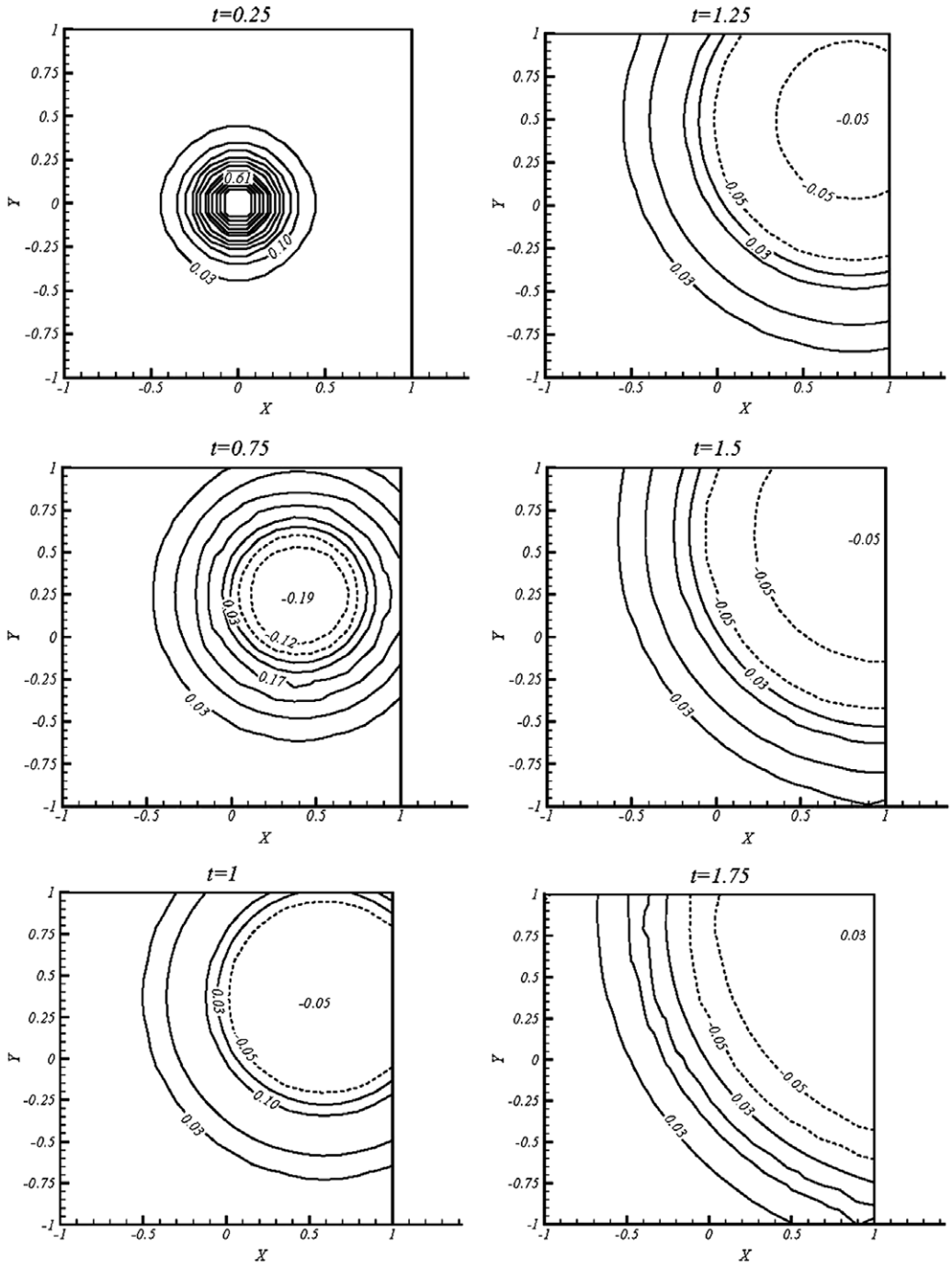

Fig. 12. Axi-symmetric pressure pulse. Pressure contours. Time evolution of the pressure pulse. $M_x = 0.8$, $M_y = 0.5$. 20×20 grid points, CFL = 0.25. Wave model B.

$$u_t + a(x) \times u_x = b(x) \times u \tag{32}$$

with $a(x) \equiv \frac{1}{2+\cos(8\pi x)}, b(x) \equiv -\sin 8\pi x,\ u(x, t=0) \equiv \sin 8\pi x\ \forall x \in [0,1]$. The boundary is 2-periodic and the exact solution of this problem is obtained from the method of characteristics. We investigate two approaches in order to solve (32). In the first approach, we locally approximate (32), at x_i, by the following form:

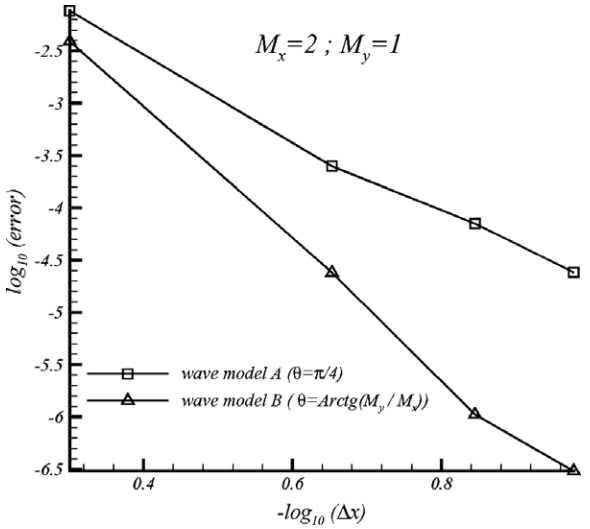

Fig. 13. Aeroacoustic equations. Grid convergence plot. Axi-symmetric pressure pulse in a non-stationary flow. Supersonic regime. $M_x = 2$, $M_y = 1$, $T = 2$.

$$u_t + a(x_i)u_x = b(x_i)u \quad \forall x \in [x_{i-1/2}, x_{i+1/2}] \tag{33}$$

Then, it becomes possible to use locally the algebraic formulae developed for the linear scalar advection [1]. The only change in these formulae concerns the parameter v (CFL), which is now locally defined as $v \equiv a(x_i) \times \Delta t/\Delta x$. The discretization is then broken up into two steps. In the first step, we use the Δ-P3 scheme developed in [1] to discretize the homogeneous form:

$$u_t + a(x_i)u_x = 0$$

This form produces a predicted numerical solution (u^*, $r^* \equiv u_x|^*$). In a second step, an ordinary differential system (ODS) is solved at each discrete value, x_i, to get the final solution (u^{n+1}, $r^{n+1} \equiv u_x|^{n+1}$). This ODS writes as

$$\left.\frac{\mathrm{d}u}{\mathrm{d}t}\right|_i^* = b(x_i) \times u|^*$$

and for the x-derivative:

$$\left.\frac{\mathrm{d}r}{\mathrm{d}t}\right|_i^* = b(x_i) \times r|^*$$

After an approximate time-integration, the resulting algebraic formulae are

$$u_i^{n+1} = \left(1 + b_i\Delta t + \frac{b_i^2}{2}\Delta t^2 + \frac{b_i^3}{6}\Delta t^3\right) \times u_i^*$$

and for the x-derivatives:

$$r_i^{n+1} = \left(1 + b_i\Delta t + \frac{b_i^2}{2}\Delta t^2\right) \times r_i^*$$

In what follows, this scheme will be referred to as the "Δ-P3 linearized" scheme. In the second approach, we discretize (32) by the methodology defining the Δ-P3 scheme, without any local simplification. Indeed, by deriving from (32) relations such as

$$r_t = -r\frac{\mathrm{d}a}{\mathrm{d}x} - ar_x + u\Delta x\frac{\mathrm{d}b}{\mathrm{d}x} + b \times r$$

and

$$u_{tt} = a^2u_{xx} + \left(a\frac{\mathrm{d}a}{\mathrm{d}x} - 2ab\right)u_x + \left(b^2 - a\frac{\mathrm{d}b}{\mathrm{d}x}\right)u$$

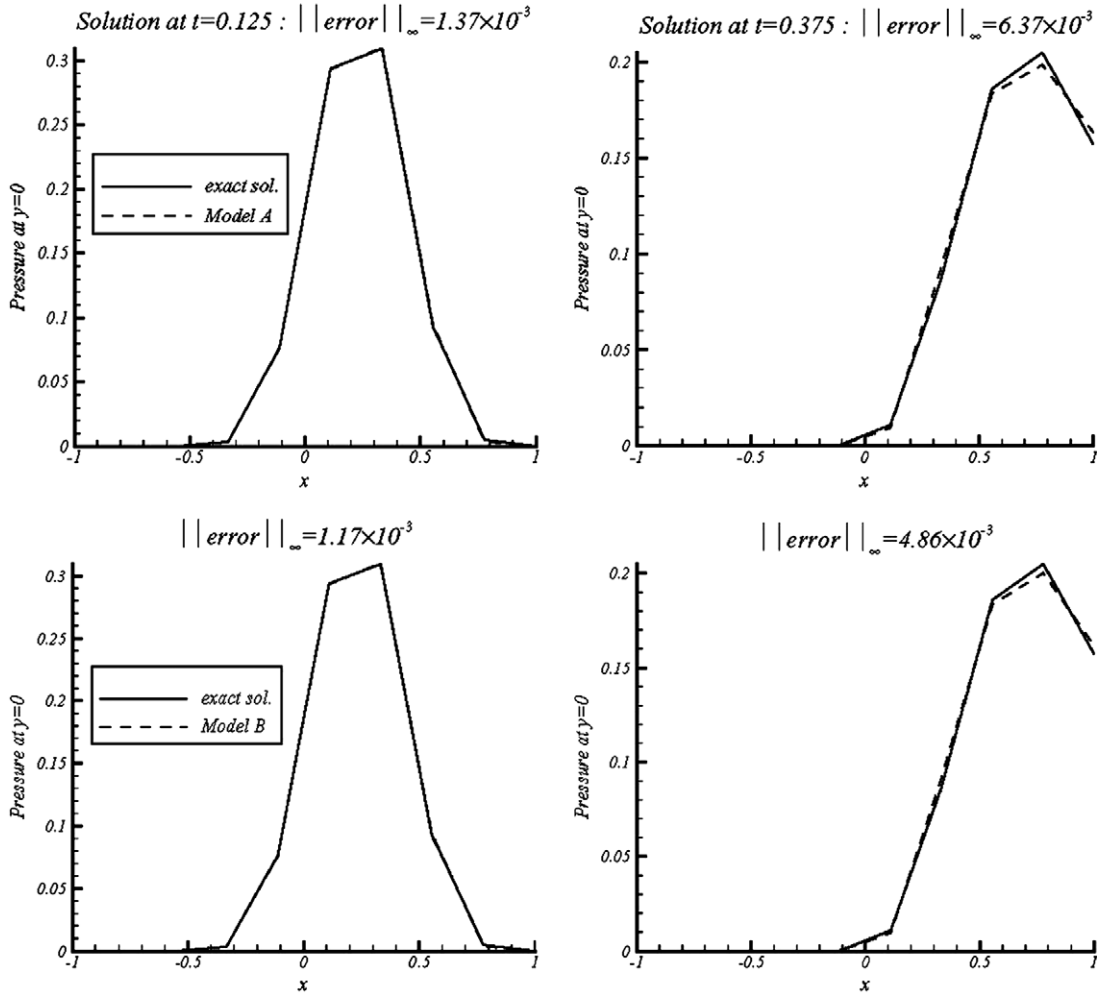

Fig. 14. Axi-symmetric pressure pulse. Pressure waveforms along the x-axis at $y = 0$. Supersonic regime: $M_x = 2$, $M_y = 1$. Top: wave model A, bottom: wave model B. 10×10 grid points, CFL = 0.25. Left: time $t = 0.5$; right: $t = 1.5$.

we can insert these relations into the time expansions for u and r. Then, we obtain the algebraic formula discretizing (32) with a third-order accuracy; strictly speaking, this is the "exact" Δ-P3 scheme for (32). For this reason, this scheme will be referred to as "Δ-P3 exact".

Even for a 1D scalar problem, this scheme is difficult to develop and very complicated to formulate. Obviously, the extension to 2D aeroacoustics is not realistic. Nevertheless, this solution is generated in order to estimate the importance of the error made by locally approximating the coefficients of (32). The numerical solutions are computed up to $T = 0.5$. All the derivatives are initialized by the zero value and we imposed CFL = 0.25 for both schemes. Fig. 16 presents the grid refinement data ($N = 20$ to 2560 cells) for the "Δ-P3 ex." and the "Δ-P3 lin." schemes. On coarse meshes, these schemes are equivalent whereas the "Δ-P3 ex." scheme reaches its designed order of accuracy on the finest meshes ($N \geqslant 640$). On the finest meshes, the "Δ-P3 lin." scheme asymptotically tends towards the value 1.5 for the slope of the plot line. Therefore, the assumption introduced into (33), although consistent with (32), does not preserve the formal order of accuracy of the Δ-P3 scheme. However, these results must be balanced by the following considerations. Firstly, we constructed the Δ-P3 scheme to be efficient on relatively coarse meshes (less than 15 cells-per-wavelength) [1]. Moreover, in realistic configurations the mean flow coefficients are usually known at discrete points (by

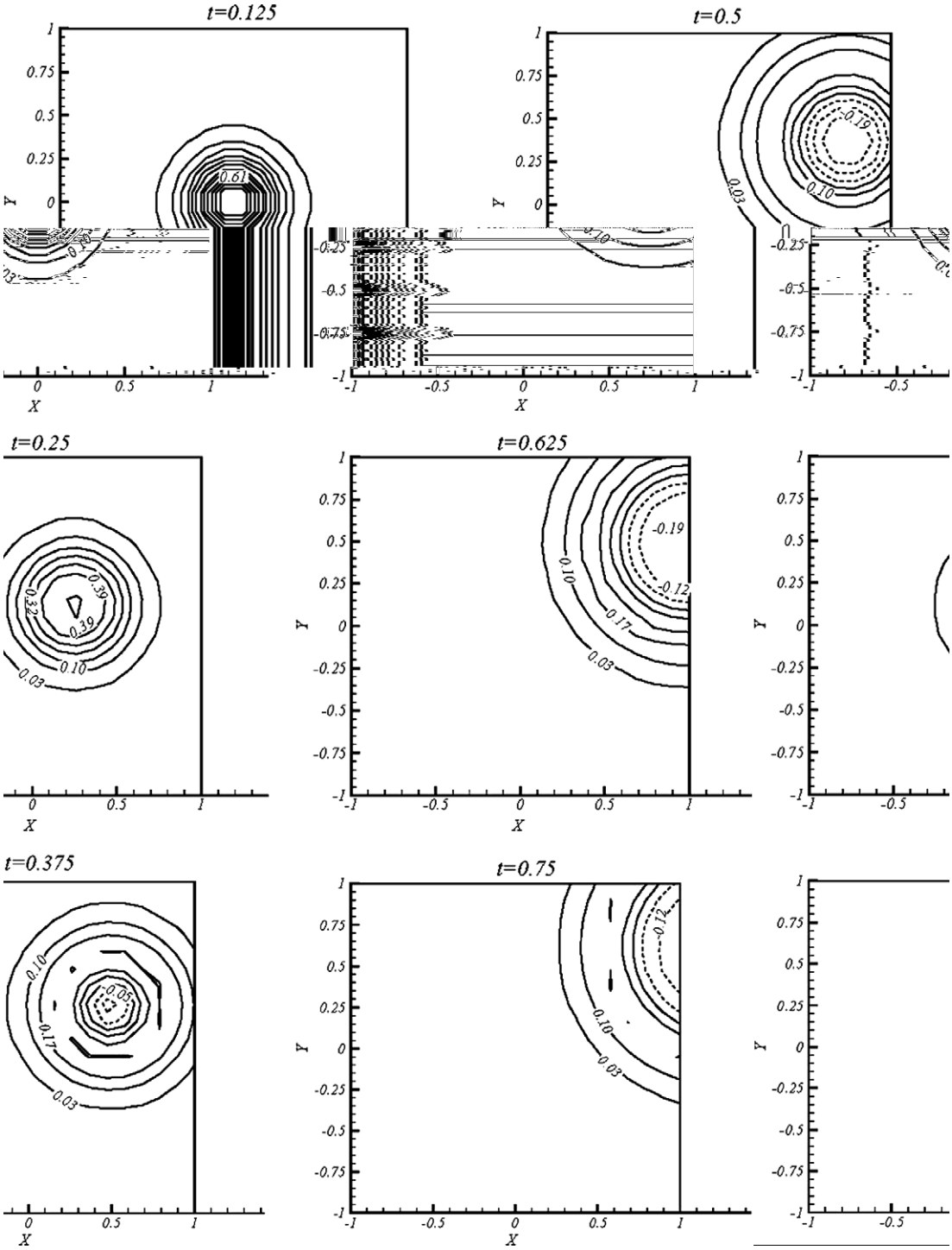

Fig. 15. Axi-symmetric pressure pulse. Pressure contours. Time evolution of the pressure pulse. $M_x = 2$, $M_y = 1$, 20×20 grid points, CFL = 0.25. Wave model B.

numerical calculations or experiments); in such a case, semi-discrete form (33) must be regarded as reference instead of the continuous form (32). For these reasons, the approximation introduced by (33) can be regarded as viable and we decided to extend this simplified methodology to the 2D aeroacoustics.

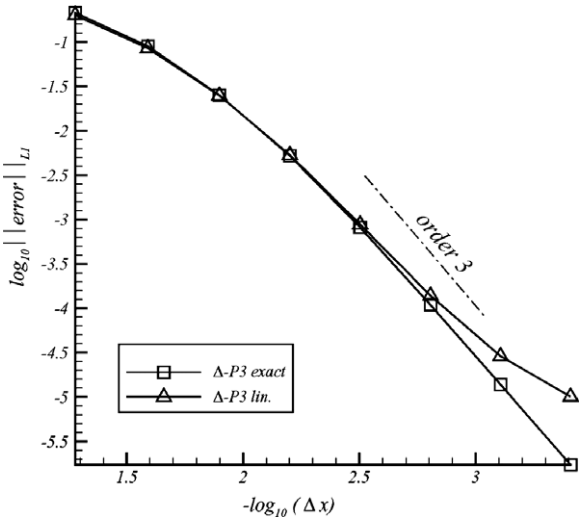

Fig. 16. Scalar model problem. Grid convergence plot. $T = 0.5$, CFL $= 0.25$. $u_t + a(x)u_x = b(x) \times u$, $a(x) = 1/(2 + \cos(8\pi x))$, $b(x) = -\sin(8\pi x)$, $u(x,t = 0) = \sin(8\pi x)$.

3.3. Generation and radiation of acoustic waves from a 2D shear layer

A thin free shear layer embracing an inflection point in the mean velocity profile is inherently unstable. Disturbances in the flow field can excite the unstable behaviour of a shear layer, if the appropriate combination of frequencies and shear layer thickness exists, causing instability waves to grow. A growing instability wave radiates noise when its phase velocity becomes supersonic relative to the ambient speed of sound. This occurs primarily when the mean jet flow is supersonic. Thus, the small disturbances in the flow, which themselves may generate noise, have resulted in an additional noise source. The main purpose of this problem is to assess the ability of our algorithm to compute this additional source of noise.

This test case is the category 5 problem of the 2000-CAA-Workshop on Benchmark problems [6]. The problem is idealized so that the exciting disturbance is a fixed known acoustic source, $S(t)$, pulsating at a single frequency, ω. The source is located inside a 2D supersonic jet with the mean flow parallel to and symmetric

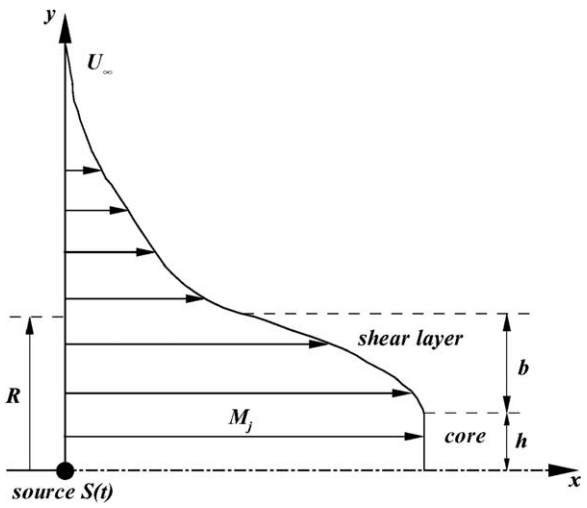

Fig. 17. Generation and radiation of acoustic waves from a 2D shear layer.

about the x-axis. Hence, the shear-layer thickness is constant, Fig. 17. With the source amplitude small enough, the problem is governed by the following set of linear equations, given in dimensionless form:

$$\begin{cases} \frac{\partial p}{\partial t} + M(y)\frac{\partial p}{\partial x} + \frac{\partial u}{\partial x} + \frac{\partial v}{\partial y} = S_p(x,y,t) \\ \frac{\partial u}{\partial t} + M(y)\frac{\partial u}{\partial x} + \frac{1}{\rho_0(y)}\frac{\partial p}{\partial x} = -v\frac{\partial M}{\partial y} \\ \frac{\partial v}{\partial t} + M(y)\frac{\partial v}{\partial x} + \frac{1}{\rho_0(y)}\frac{\partial p}{\partial y} = 0 \end{cases} \tag{34}$$

The variables are non-dimensionalized by the mean values at the jet centreline, namely, the speed of sound a_j for the velocity, ρ_j for density, $\rho_j a_j^2$ for the pressure and the half velocity distance from the x-axis, R (see [6] for more details). The parallel mean velocity profile is as follows:

$$M(y) = \begin{cases} M_j \times \mathrm{e}^{-6.25\times Log2\times(y-b)^2} & y \geqslant h \\ M_j & y \leqslant h \end{cases} \tag{35}$$

and the mean density profile is related to the axial velocity by the following relation:

$$\frac{1}{\rho_0(y)} = -\frac{\gamma-1}{2}M(y)\times(M(y)-M_j) + \frac{M(y)}{M_j}\times\left(1-\frac{\rho_j}{\rho_\infty}\right) + \frac{\rho_j}{\rho_\infty} \tag{36}$$

$S_p(x, y, t)$ stands for the acoustic source exciting instability waves in the shear layer. This source term takes the form:

$$S_p(x,y,t) = A\times \mathrm{e}^{-B\times Log(x^2+y^2)}\times\cos\omega\times t \tag{37}$$

The constants are set as follows: $h = 0.6$ (width of the uniform core), $b = 0.4$, $\rho_j = 1$, $\rho_\infty = 0.556$, $M_j = 2$ (Mach number of the jet), $A = 2.723\times10^{-11}$, $B = 8$. This problem is parametrized by the Strouhal number, S_{tr}, defined by

$$S_{tr} \equiv \frac{\omega}{\pi\times M_j}$$

We solve this problem for the forcing frequency: $S_{tr} = 0.14$. For this Strouhal number, the acoustic perturbation excites a growing instability wave; the pressure fluctuations are convected with amplification in the shear-layer. Then, the radiated field is mainly due to this instability wave. In the core of the supersonic jet, the wave-lengths of the fastest and slowest acoustic waves, $\lambda^{\pm}/R$ are

$$\frac{\lambda^{\pm}}{R} = \left(1\pm\frac{1}{M_j}\right)\times\frac{2}{S_{tr}}$$

and for the shear wave:

$$\frac{\lambda^0}{R} = \frac{2}{M_j\times S_{tr}}$$

Therefore, for $S_{tr} = 0.14$ and $M_j = 2$, the characteristic acoustic and shear wave-lengths of this problem, are:

$$\frac{\lambda^-}{R} = \frac{\lambda^0}{R} = 7.14, \quad \frac{\lambda^+}{R} = 21.43 \tag{38}$$

Exact solutions for the sound intensities, $\overline{p^2}$, along $y = 10$ and $x = 50$, are reported in [10] and provide a standard for evaluating the characteristics of the numerical solution. This problem is locally simplified by using the procedure tested in Section 3.2. Then, for each discrete point (x_i, y_i), we solve the following linear system:

$$\begin{cases} \frac{\partial p}{\partial t} + M(y_i)\frac{\partial p}{\partial x} + \frac{\partial u}{\partial x} + \frac{\partial v}{\partial y} = S_p(x,y,t) \\ \frac{\partial u}{\partial t} + M(y_i)\frac{\partial u}{\partial x} + \frac{1}{\rho_0(y_i)}\frac{\partial p}{\partial x} = S_u(x,y,t) \\ \frac{\partial v}{\partial t} + M(y_i)\frac{\partial v}{\partial x} + \frac{1}{\rho_0(y_i)}\frac{\partial p}{\partial y} = 0 \end{cases} \tag{39}$$

The source term for the perturbation velocity, u, is defined as follows: $S_u(x, y, t) \equiv -v \times \partial M/\partial y$. Therefore, by doing the identifications: $M_x \equiv M(y_i)$ and $M_y \equiv 0$, we can employ in a direct way the formulae previously derived to produce the Δ-P3 scheme, in order to discretize (39). Since $M_y \equiv 0$, wave model B is simplified by employing formulae (16). Then, the numerical solution is updated, in the prediction step, by using (17), according to the process depicted in Fig. 6. Wave model A remains unchanged for this problem. The non-reflecting boundary conditions derived in Section 2.4 are applied at the subsonic boundaries by setting the waves entering the computation domain to zero, while the waves leaving this domain are used to update the boundary values. At the supersonic inflow, all variables are put at zero (no ingoing perturbations). Due to symmetry in the mean flow and the presence of the source term, S_p, only the solution in the upper half plane is computed. Therefore, symmetry conditions are applied for u, v, p and its derivatives at every point, S, located on the x-axis. These conditions are the following:

$$\begin{aligned} &v|_S \equiv 0, r_v|_S \equiv 0 \\ &s_u|_S \equiv 0, s_p|_S \equiv 0 \end{aligned} \tag{40}$$

The remaining variables are updated by the simple waves leaving the computation domain along the x-axis. The computation domain is defined by the conditions: $-5 \leqslant x \leqslant 60$ and $0 \leqslant y \leqslant 12$.

One of the main difficulties of simulating a shear layer in such a large computation domain lies in different solution requirements in various regions. Usually, the grid must be fine enough to capture the sound generation process across the thin shear-layer, whereas this grid can be relatively coarse in the propagation region.

To simplify, we use a uniformly distributed mesh size, Δx, in the x-direction. The mesh is geometrically stretched in the y-direction in order to place more grid points between $y = 0.6$ and $y = 1.8$, where $\partial M/\partial y$ is large and the perturbation solution varies significantly. Indeed, it appeared throughout these computations that the numerical solution was very sensitive to the stretching of the grid. The numerical solutions that we present below try to give the best compromise between the exactitude and the stability of the scheme. Formula (30) is modified to take account of the non-uniformity of the mesh. Then, the discrete time-step, Δt, is calculated by

$$\Delta t \equiv \mathrm{CFL} \times \min_i \left[\sqrt{\frac{\Delta x \Delta y_i}{\pi}} \times \frac{1}{1 + M(y_i)} \right] \tag{41}$$

Computations are run up to the dimensionless time $T = 50$, until the numerical solution becomes periodic in time.

First, let us consider the numerical results obtained in using wave-model A ($\theta \equiv \pi/4$). Fig. 18 shows the mean quadratic fluctuations of the pressure, $\overline{p^2}$ (averaged over one period), along both lines $y = 10$ and $x = 50$. For this simulation, 120×60 grid points are used (120 points in the x-direction). The mesh is stretched in such a way that eight cells are located in the region $0.6 \leqslant y \leqslant 1.8$. The CFL number is taken equal to 0.25, the size of the time-step is equal to $\Delta t = 1 \times 10^{-2}$ and the required CPU time is 400 s. Considering the characteristic wave-lengths, (38), this grid resolution is equivalent to 13 points per wave-length for the slowest wave and 40 points per wave-length for the fastest one. As one can note it from Fig. 18, the calculated sound intensity along $y = 10$ shows an exponential increase of the acoustic intensity along the downstream direction; this implies that the acoustic source inside the jet has excited an instability wave. This wave has generated and radiated amplified sound field along the downstream direction. Thus, these numerical results are consistent with the physical solution. Comparisons with the exact solution confirm this point. Indeed, the sound intensity is in close agreement with the exact solution at $x = 50$, while it is underestimated at $y = 10$, mostly near the acoustic source. This suggests that the grid may need further refinement at the jet core.

Consequently, we present a new simulation with 150×75 grid points, Fig. 19. For this resolution, 14 cells are located within the physical range $0.6 \leqslant y \leqslant 1.8$. This grid resolution is nearly equivalent to 17 points per wavelength for the slowest wave and 50 points for the fastest one. The CFL number is equal to 0.30. The time-step is now $\Delta t = 7 \times 10^{-3}$ and the required CPU time is 750 s to reach the simulation time $T = 50$. Differences are perceptible between Figs. 18 and 19: the level of the mean square pressure along the line $y = 10$ is improved for $x \geqslant 25$, when one considers the 150×75 mesh; however, the rapid growing of the sound intensity level in the source region remains insufficiently captured. Moreover, the capturing of the exponential growing of the instability wave across the shear-layer is not improved since

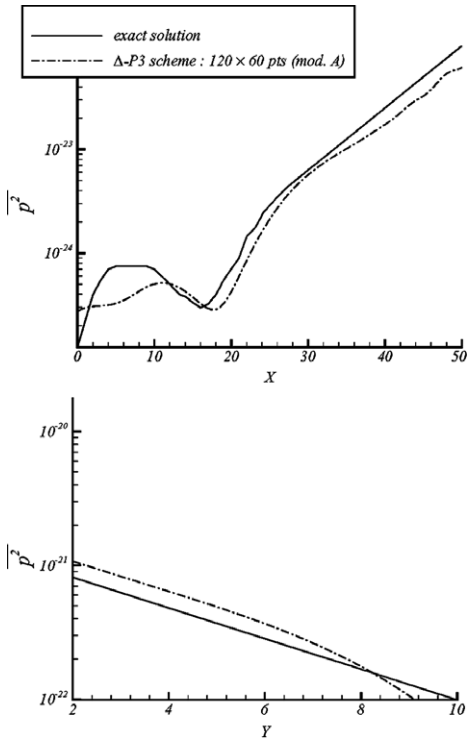

Fig. 18. 2D shear layer. Δ-P3 scheme: intensity of radiated sound, $\overline{p^2}$, averaged over one period, along $y = 10$ (top) and $x = 50$ (bottom). 120×60 grid points – wave model A (CFL = 0.25).

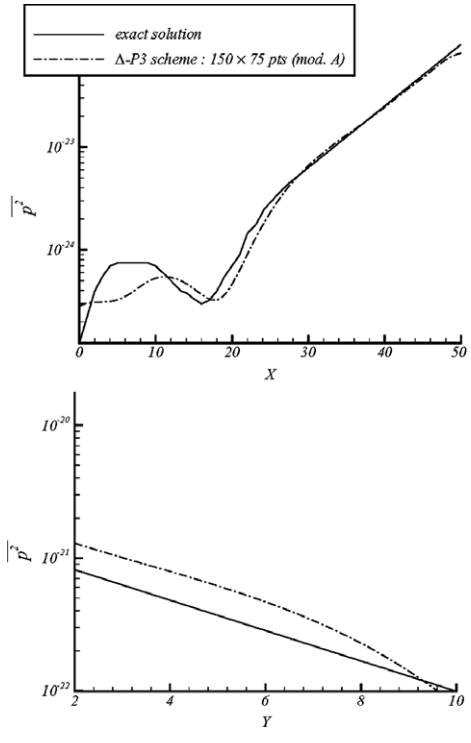

Fig. 19. 2D shear layer. Δ-P3 scheme: intensity of radiated sound averaged over one period. 150×75 grid points – wave model A (CFL = 0.30).

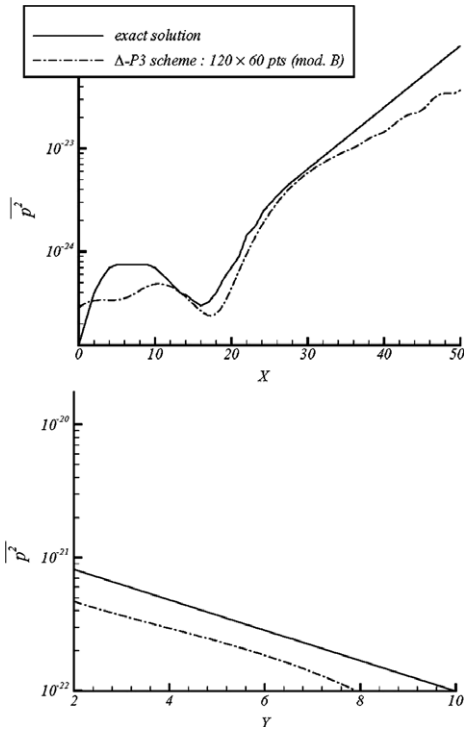

Fig. 20. 2D shear layer. Δ-P3 scheme: intensity of radiated sound averaged over one period. 120×60 grid points – wave model B (CFL = 0.60).

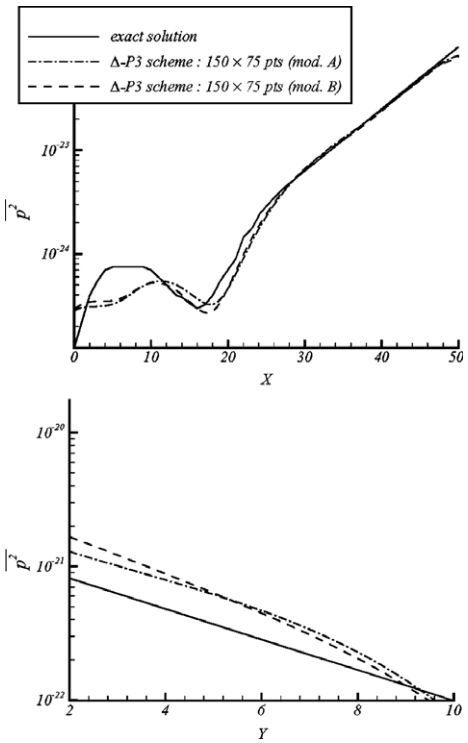

Fig. 21. 2D shear layer. Δ-P3 scheme: intensity of radiated sound averaged over one period. 150×75 grid points – comparisons between wave models A and B along $y = 10$ (top) and $x = 50$ (bottom).

the sound intensity level is slightly higher at $x = 50$, in comparison with Fig. 18. This is a problem due to the stretching of the grid: if one modifies this stretching, one can improve the solution at $x = 50$, but then this change deteriorates the solution at $y = 10$. Clearly, the resolving power of this mesh is still insufficient for the whole computation domain.

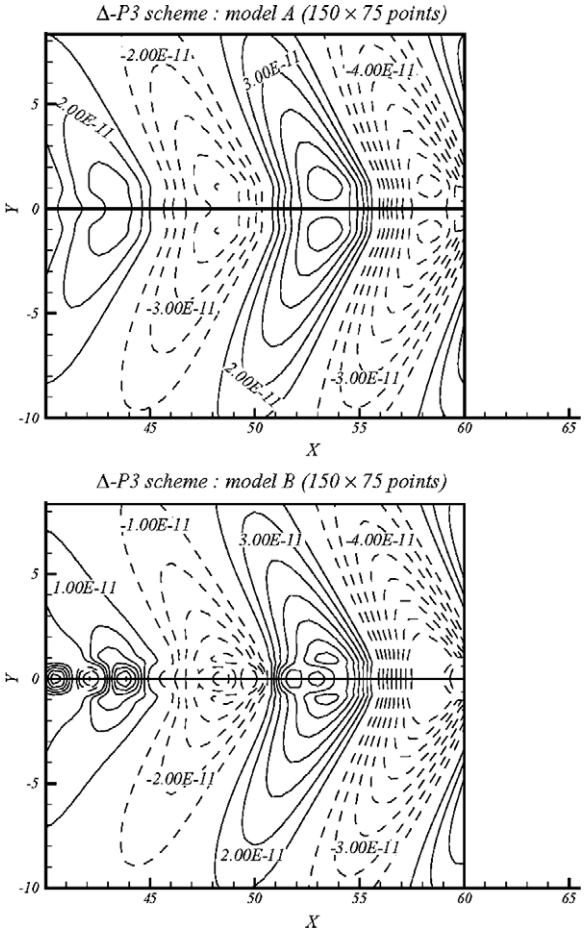

Fig. 23. 2D shear layer. Δ-P3 scheme: instantaneous pressure contours at $T = 50$. Zoom in the region of the outflow/radiation boundary. 15 isolines from 7×10^{-11} to -8×10^{-11}. Top (model A, CFL = 0.30); bottom (model B, CFL = 0.60).

jet are undeniably noticeable with model B, Figs. 22 and 23, while these pulses are strongly attenuated with model A. Therefore, instantaneous pressure contours are more indicative of the dissipative nature of model A than the sound intensity levels.

If we summarize these first results, one can conclude that wave-model B is more efficient in terms of CPU time since its numerical stability domain is larger and its algebraic complexity is lesser for this kind of problem (formulae (16)); moreover, it is less dissipative since the propagation of simple waves is designed to follow the mean flow characteristics. This latter point is not perceivable when one considers mean square pressure profiles. Indeed, by only considering the pressure profiles, wave model A seems to be more advantageous on a coarse grid (Figs. 18 and 20).

However, these results must be improved since the numerical solution strongly depends on the stretching of the mesh. Fig. 24 exhibits numerical results for 175×100 grid points. This grid resolution is nearly equivalent to 19 points per wavelength for the slowest wave and 57 points for the fastest one. With a CFL number taken equal to 0.60, the CPU time required is now 792 s. The time-step size is equal to$\Delta t = 2.1 \times 10^{-2}$. Now, the growing of the sound intensity along the line $x = 50$ is very close to the exact one, while the sound intensity along $y = 10$ is unchanged in comparison with Fig. 21. Moreover, the numerical solution becomes less sensitive to the stretching of the mesh. However, the grid resolution is still insufficient to exactly capture the characteristics of the source region.

To end this section, we compare the Δ-P3 scheme with a more classical numerical method specifically developed for CAA computations: the 7-point stencil Dispersion–Relation-Preserving (DRP) scheme of Tam and

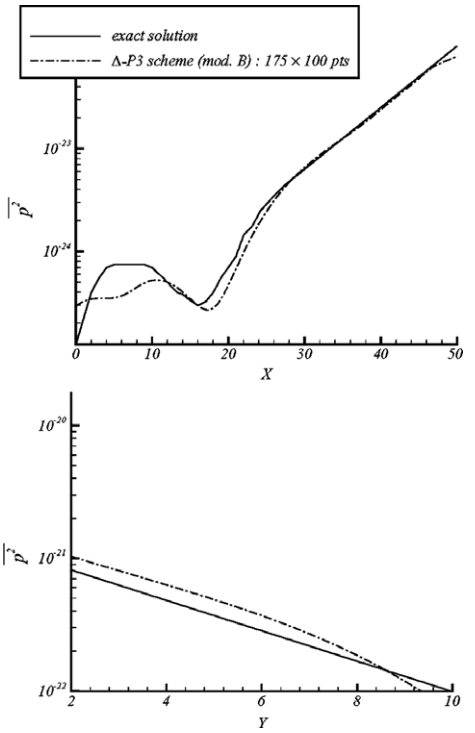

Fig. 24. 2D shear layer. Δ-P3 scheme: Intensity of radiated sound averaged over one period. 175×100 grid points – wave model B (CFL = 0.60).

Webb [8]. This method is employed for discretizing (39). The time integration is performed by a six step Runge–Kutta algorithm: the low-dissipation and low-dispersion Runge–Kutta (LDDRK6) scheme by Hu et al. [14]. At the inflow at $x = -5$, Tam and Webb asymptotic radiation conditions [8] are used for the subsonic region ($3 < y \leqslant 12$):

$$\left(\frac{1}{V(\theta)} \times \frac{\partial}{\partial t} + \frac{\partial}{\partial r} + \frac{1}{2r}\right) \begin{bmatrix} u \\ v \\ p \end{bmatrix} = 0$$

where $V(\theta) \equiv [M\cos\theta + \sqrt{(1 - M^2 \sin^2\theta)}]$. θ is the angular coordinate of the boundary point and r is the distance of this point from the source. In the supersonic region ($0 \leqslant y \leqslant 3$), all the perturbed quantities are set to zero. At the far-field boundary ($y = 12$), Tam and Webb asymptotic radiation conditions are specified. At the outflow ($x = 60$), the outflow boundary conditions by Tam and Webb are implemented [8]:

$$\begin{cases} \frac{1}{V(\theta)}\frac{\partial p}{\partial t} + \cos\theta\frac{\partial p}{\partial x} + \sin\theta\frac{\partial p}{\partial y} + \frac{p}{2r} = 0 \\ \frac{\partial u}{\partial t} + M\frac{\partial u}{\partial x} = -\frac{\partial p}{\partial x} \\ \frac{\partial v}{\partial t} + M\frac{\partial v}{\partial x} = -\frac{\partial p}{\partial y} \end{cases}$$

A symmetric boundary condition is applied at $y = 0$: $v = 0$, $\partial/\partial y[u,p]^t = 0$. All the space derivatives are upwinded according to the fourth-order algebraic formulae:

$$\left.\frac{\partial \varphi}{\partial x}\right|_i^- = \frac{1}{\Delta x}\left[\frac{24}{156}\varphi_i - \frac{28}{13}\varphi_{i-1} + \frac{7}{13}\varphi_{i-2} + \frac{4}{39}\varphi_{i-3} - \frac{3}{52}\varphi_{i-4}\right]$$

$$\left.\frac{\partial \varphi}{\partial x}\right|_i^+ = \frac{1}{\Delta x}\left[-\frac{25}{12}\varphi_i + 4\varphi_{i+1} - 3\varphi_{i+2} + \frac{4}{3}\varphi_{i+3} - \frac{1}{4}\varphi_{i+4}\right]$$

Furthermore, in order to stabilize the numerical procedure, we adopt the selective artificial damping method [2] for eliminating short wavelength spurious waves. We used the following sixth-order dissipative term:

$$D_i = -\mu \sum_{j=-3}^{j=3} c_j \times \varphi(x_i + j\Delta x)$$

with

$$c_0 = 0.3276986608, \quad c_1 = c_{-1} = -0.235718815, \quad c_2 = c_{-2} = 0.0861506696, \quad c_3 = c_{-3} = -0.0142811847$$

For all these simulations, we selected: $\mu = 1 \times 10^{-2}$, which ensures the best compromise between accuracy and stability. This dissipative term is added for all the variables u, v, p. We perform all the computations on a uniformly distributed mesh. A CFL equal to 0.5 is used in all simulations.

Fig. 25 gives the calculated sound intensities along $y = 10$ and $x = 50$ at the dimensionless time $T = 50$. The number of grid points is 120×60 points in the x- and y-directions, respectively, and the CPU time is equal to 50 s. Compared with the results given by the Δ-P3 scheme (model B) on the same mesh, the lack of resolution of the DRP scheme is obvious. This lack of resolution is especially true in the source region and at the outflow boundary.

On a finer grid (175×100 grid points), Fig. 26 compares the results obtained by the DRP ($t_{\mathrm{CPU}} = 210$ s) and Δ-P3 schemes ($t_{\mathrm{CPU}} = 792$ s); the DRP scheme still underestimates the solution at $y = 10$. Fig. 27 compares the DRP scheme on the finest grid (175×100 grid points) with the numerical solution obtained by the Δ-P3 scheme on a coarser grid (120×60 grid points, $t_{\mathrm{CPU}} = 170$ s). Thus, with roughly the same CPU time, the Δ-P3 scheme produces numerical results similar to those obtained with the DRP scheme. However, one can note that the source region remains badly described by both schemes.

Lastly, Fig. 28 compares the instantaneous pressure contours in the region close to the symmetry line and the exit boundary, for the DRP and Δ-P3 schemes on a 175×100 grid. The dispersive nature of the DRP

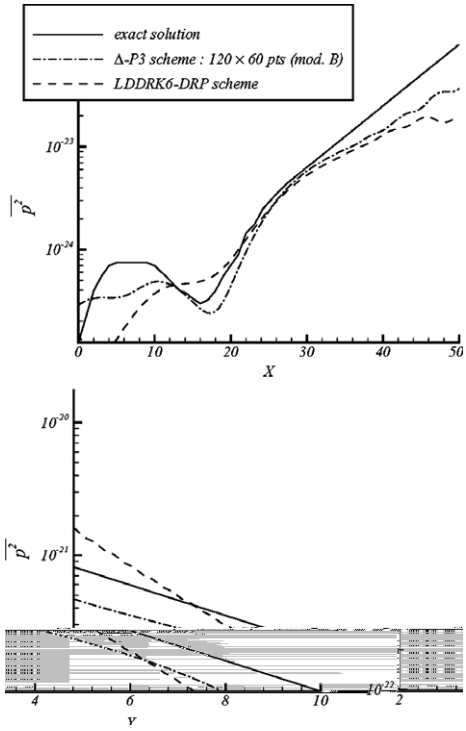

Fig. 25. 2D shear layer. Comparisons between LDDRK6-DRP scheme (CFL = 0.50) and Δ-P3 scheme (model B, CFL = 0.60): intensity of radiated sound averaged over one period, along $y = 10$ (top) and $x = 50$ (bottom). 120×60 grid points.

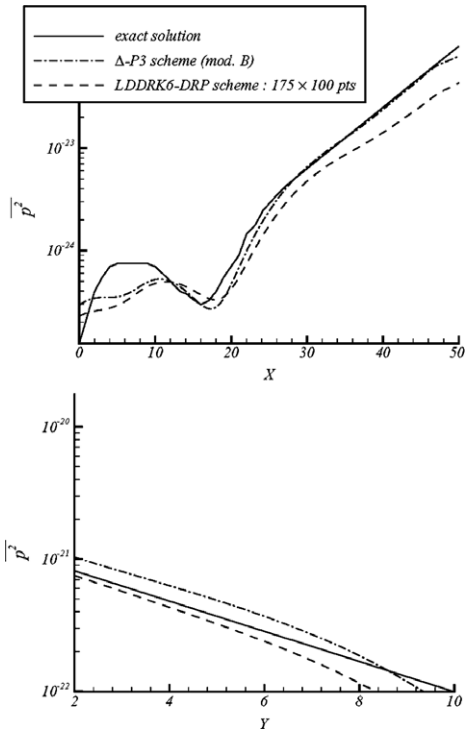

Fig. 26. 2D shear layer. Comparisons between LDDRK6-DRP scheme (CFL = 0.50) and Δ-P3 scheme (model B, CFL = 0.60): Intensity of radiated sound averaged over one period, along $y = 10$ (top) and $x = 50$ (bottom). 175×100 grid points.

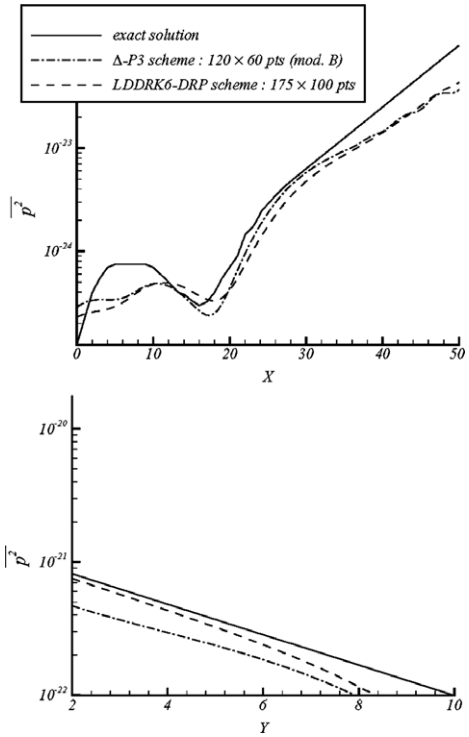

Fig. 27. 2D shear layer. Intensity of radiated sound averaged over one period along $y = 10$ (top) and $x = 50$ (bottom): comparisons between Δ-P3 scheme (120×60 grid points, CFL = 0.60, model B) and LDDRK6-DRP scheme (175×100 grid points, CFL = 0.50).

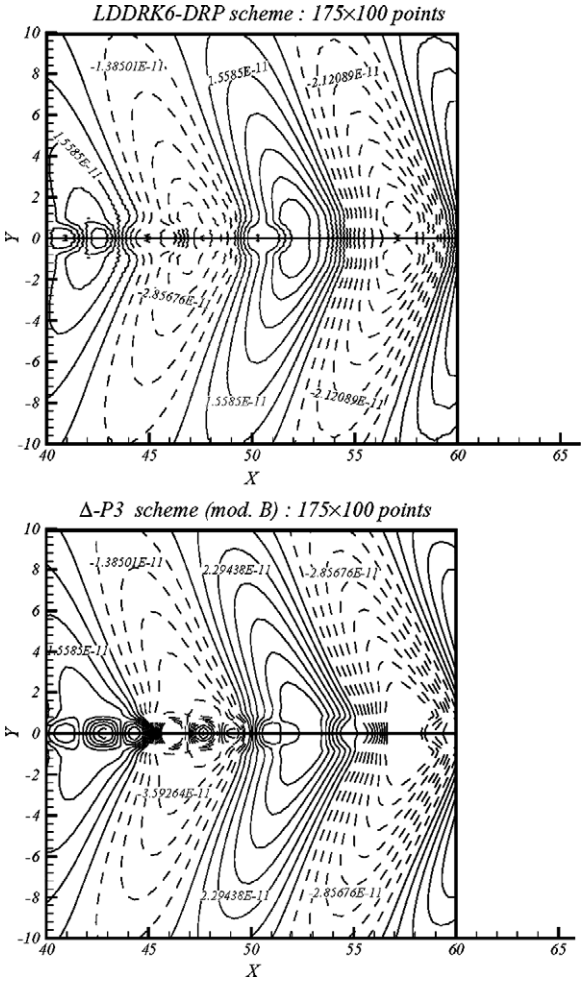

Fig. 28. 2D shear layer. Instantaneous pressure contours at $T = 50$. Zoom in the region of the outflow/radiation boundary. 175×100 grid points. 15 isolines from 4.50×10^{-11} to -5.8×10^{-11}. Top (LDDRK6-DRP scheme, CFL = 0.50); bottom (Δ-P3 scheme, model B, CFL = 0.60).

scheme and its lack of resolution near the symmetry line clearly appear. To be more quantitative, we have counted the number of floating point operations needed per grid points for each scheme; the Δ-P3 scheme needs 8×10^5 operations per grid point to perform these computations while the DRP scheme only necessitates 5×10^5operations. In addition, the required memory (storage location per variable per grid point) is equal to 1.4×10^{-4} Mo for the Δ-P3 scheme while it is 9.3×10^{-5} Mo for the DRP scheme. Obviously, these last results clearly demonstrate that a Hermitian method with high resolution on relatively coarse meshes generates a computational cost higher than that of a more traditional method.

However, this drawback must be balanced by the following remarks:

- For roughly the same accuracy and the same CPU time (Fig. 27), the Δ-P3 scheme requires 1Mo per variable while the DRP scheme necessitates 1.5 Mo (see [11–13] for more numerical comparisons).
- Owing to the compactness and the upwind nature of the numerical stencil, boundary conditions are treated in an easier way when one employs the Δ-P3 scheme; there is no need to use additional numerical techniques such as artificial damping terms, ghost points, grid stretching or asymptotic solutions.
- Lastly, because of its very compact nature, the Δ-P3 scheme is well suited for an efficient parallelization; thus, the computational effort can still be appreciably reduced.

4. Conclusions

A compact Hermitian and upwind scheme for discretizing the linear aeroacoustics has been put forward and surveyed in this paper. The principal idea of the method lies in a decomposition in three stages of the discretization, namely: the reconstruction, the decomposition and the evolution stages. In a previous paper [1], we have experimented the reconstruction and the evolution stages. This paper concentrates on the decomposition stage and the associated boundary conditions, in order to compute linear aeroacoustic problems. By using a six-wave model to decompose the time-derivatives, we can distinguish the time-fluctuations associated with each wave.

By defining a propagation direction independent of the numerical data, the problem remains linear. The discrete variables and its derivatives can be updated simultaneously while following the sign of each wave speed. Due to the linear nature of the problem, the variables and its derivatives are updated by the same waves. The enlargement to non-uniform mean flow is ensured by a local linearization. Although this approach does not preserve the formal high order of accuracy of the scheme, it is shown to give very accurate results which bear comparison with a ''state of the art'' high resolution scheme on coarse meshes. Thus, the best six-wave model (four acoustic and two shear waves), when a supersonic uniform background flow exists, is obtained with a propagation angle depending on the local mean flow direction (''wave model B''). In the subsonic areas, waves A and B give similar results.

The advantage of using such a procedure is twofold: first, the wave propagation is treated in a multi-dimensional way, free of the grid topology; second the scheme so generated is highly compact, promoting the treatment of specific boundary conditions and effective parallelization.

Once the wave model is defined, specific non-reflecting boundary conditions based on the waves crossing a given boundary can be derived. These conditions generate algebraic relations at the boundary points. In doing so, we can generate a third-order Hermitian scheme, namely the ''Δ-P3 scheme''. Although slightly dissipative (more than 10 points per wave length are needed), the Δ-P3 scheme is appealing since its upwind nature provides an intrinsic numerical dissipation which damps out numerical instabilities created at the boundaries or by grid irregularities. The test-case of the 2D shear-layer seems to validate this last point. To conclude, we must insist on the following result: the algebraic complexity introduced by a Hermitian technique is balanced by a greater accuracy on coarse meshes.

Therefore, we can hope that introducing the second derivatives of the solution as unknowns could further increase this effectiveness. This solution can be worthwhile if we reduce algebraic complexity by using a process of Runge–Kutta instead of a procedure of Cauchy–Kovaleskaya; this point will be investigated in the immediate future in order to improve the resolving power of this algorithm and to extend its capacities to 3D computations.

Acknowledgement

The author gratefully thanks Dr. G.B. Deng (Ecole Centrale de Nantes – France) for providing helpful technical support throughout this work.

References

[1] G. Capdeville, A new category of Hermitian upwind schemes for computational acoustics, J. Comput. Phys. 210 (2005) 133–170.
[2] C.K.W. Tam, Computational aeroacoustics: issues and methods, AIAA J. 33 (10) (1995) 1788–1796.
[3] A. Majda, Compressible Fluid Flow and System of Conservation Laws in Several Space Variables, Springer Verlag, 1984.
[4] H. Deconinck, Analysis of wave propagation properties for the Euler equations in two space dimensions, in: VKI-Lecture Series on Computational Fluid Dynamics, March 21–25, 1994.
[5] C.K.W. Tam, Advances in numerical boundary conditions for computational aeroacoustics, AIAA Paper, 97-1774, 1997.
[6] Third Computational Aeroacoustics Workshop on Benchmark Problems, NASA/CP-2000-209790, 2000.
[7] S.K. Lele, Computational aeroacoustics: a review, AIAA Paper, 97–0018, 1997.
[8] C.K.W. Tam, J.C. Webb, Dispersion–relation-preserving finite difference schemes for computational acoustics, J. Comput. Phys. 107 (1993) 262–281.
[9] S.K. Lele, Compact-finite difference schemes with spectral-like resolution, J. Comput. Phys. 103 (1992) 16–42.

[10] M.D. Dahl, Solution to the category 5 problem: generation and radiation of acoustic waves from a 2D shear layer, in: Third CAA Workshop on Benchmark Problems, NASA/CP-2000-209790, 2000, pp. 87–92.
[11] D.P. Lockard, H.L. Atkins, An application of the quadrature-free discontinuous Galerkin method, in: Third CAA Workshop on Benchmark Problems, NASA/CP-2000-209790, 2000, pp. 331–338.
[12] T.E. Scheidegger, P.J. Morris, Generation and radiation of acoustic waves from a 2D shear layer, in: Third CAA Workshop on Benchmark Problems, NASA/CP-2000-209790, 2000, pp. 315–322.
[13] X. Li, F. Thiele, Numerical computation of the generation and radiation of acoustic waves from a 2D shear layer, in: Third CAA Workshop on Benchmark Problems, NASA/CP-2000-209790, 2000, pp. 323–329.
[14] F.Q. Hu, M.Y. Hussaini, J. Manthey, Low-dissipation and -dispersion Runge–Kutta schemes for computational acoustics, J. Comput. Phys. 124 (1996) 177.
[15] P.L. Roe, Discrete models for the numerical analysis of time dependant multi-dimensional gas dynamics, J. Comput. Phys. 63 (1986) 458–476.